coatings

MDPI

Article

A Strategy of Candle Soot-Based Photothermal Icephobic Superhydrophobic Surface

Chenlu Qian †, Lu Wang †, Qiang Li * and Xuemei Chen *

MIIT Key Laboratory of Thermal Control of Electronic Equipment, School of Energy and Power Engineering, Nanjing University of Science and Technology, Nanjing 210094, China; qianchenlu359@163.com (C.Q.); wanglullaby@163.com (L.W.)

* Correspondence: liqiang@njust.edu.cn (Q.L.); xuemeichen@njust.edu.cn (X.C.)

† These authors contributed equally to this work.

Abstract: Anti-icing/de-icing is of fundamental importance in practical applications such as power transmission, wind turbines, and aerofoils. Despite recent efforts in developing engineering surfaces to delay ice accumulation or reduce ice adhesion, it remains challenging to design robust photothermal icephobic surfaces in a durable, low-cost, easy-fabrication manner. Here, we report an intelligent candle soot-based photothermal surface (PDMS/CS60@PDMS/Al) that can utilize sunlight illumination to achieve the multi-abilities of anti-icing, de-icing, and self-cleaning. Our method lies in the construction of hierarchical micro/nanostructures by depositing photothermal candle soot nanoparticles, which endow the surface with superior superhydrophobicity and excellent photothermal performance. The underlying mechanism is exploited by establishing the heat transfer model between the droplets and the cooled surface. We believe that the smart PDMS/CS60@PDMS/Al developed in this work could provide a feasible strategy to design intelligent engineering surfaces for enhanced anti-icing/de-icing.

Keywords: candle soot; photothermal; icephobic; superhydrophobic; sun illumination

Citation: Qian, C.; Wang, L.; Li, Q.; Chen, X. A Strategy of Candle Soot-Based Photothermal Icephobic Superhydrophobic Surface. *Coatings* **2024**, *14*, 612. https://doi.org/10.3390/coatings14050612

Academic Editor: Ludmila B. Boinovich

Received: 9 April 2024
Revised: 9 May 2024
Accepted: 10 May 2024
Published: 12 May 2024

1. Introduction

Ice formation and accumulation is a ubiquitous and unavoidable phenomenon that exists in numerous engineering fields, including power transmission, refrigeration, wind turbines, and aerofoils [1–3]. For instance, the occurrence of ice accretion on wind turbines in harsh environments can lead to a loss of up to 50% of the annual production [4]. Hence, it is urgent to develop effective and reliable anti-icing/de-icing strategies. The traditional strategies to mitigate ice accumulation after freezing include electrothermal de-icing [5], chemical de-icing [6], and mechanical de-icing [7]. Despite the fact that ice on cold surfaces can be removed by Joule heating or mechanical vibrations, these methods are all energy-consuming, inefficient, and eco-unfriendly [8,9].

Recent advances in micro/nanotechnology and surface functionality have spurred the development of intelligent engineering surfaces to prevent ice nucleation, delay ice accumulation, and reduce ice adhesion after freezing. Manna et al. [10] summarize the various reports published over the years that have elaborated on the distinctive importance of both chemistry and topography in imparting and modulating various bio-inspired wettability. Some strategies have been proposed to design the slippery liquid-infused porous surface (SLIPS), targeting reducing ice adhesion once freezing happens [11,12]. The SLIPS is created by infiltrating the micro/nanostructured porous structures with a lubricating fluid. The lubricant on the SLIPS is immiscible in most aqueous solutions and effectively blocks the direct contact between the droplet and the surface. When ice forms on the SLIPS, ice adhesion is extremely low due to the existence of the lubricant layer. However, the SLIPS would lose anti-icing/de-icing properties once the lubricant layer was depleted [13,14].

Therefore, the SLIPS may not be durable for practical applications. Some other strategies have been adopted to construct micro/nanostructures on superhydrophobic surfaces, aiming to delay ice nucleation. It is reported that the superhydrophobic surface with hierarchical micro/nanostructures can delay ice nucleation and decrease ice accumulation by reducing the contact area between droplets and the surface [15–17]. Unfortunately, ice can simply form on the superhydrophobic surface under subzero-degree conditions. Once ice interlocks with the micro/nanostructures, the superhydrophobic surface loses its workability, leading to an increased ice adhesion force [18,19]. It is well known that the utilization of photothermal materials such as plasmonic particles, magnetic particles, and carbon nanomaterials to construct functional surfaces that can generate heat via light illumination [20,21]. Combined with superhydrophobicity, the photothermal surface can prevent ice nucleation, delay ice accumulation, and even melt accumulated ice layers [22,23]. This endows the photothermal surface with robust abilities for both anti-icing and de-icing in extreme environments [24–27]. Miao et al. [28] reported a facile strategy of employing ice crystals to construct sophisticated hierarchical micro-nanostructured anti-icing composites with photothermal, self-healable, and self-cleaning properties. However, few of them succeed in solving the problems of high-cost or ultra-complex fabrications.

More recently, candle soot nanoparticles have gotten enormous attention because of their inexpensive and photothermal performance. Extensive studies have proved that the candle soot-based surface can achieve superhydrophobic and photothermal icephobic performance [29–31]. The candle soot-based superhydrophobic photothermal surfaces can maintain a long-term ice-free state for the entire surface under the sun's illumination in a low-temperature environment. For example, the surface temperature of a candle soot-based superhydrophobic photothermal surface can increase by 53 °C under 1-sun illumination [31]. It relies on the excellent photothermal performance of candle soot on the micro/nanostructures of the surface. Obviously, the construction of the hierarchical micro/nanostructures is crucial to the robust anti/deicing ability of the candle soot-based photothermal superhydrophobic surface. However, most candle soot-based photothermal coatings tend to be unstable, and candle soot particles tend to fall off the coatings when impacted by water droplets or soaked in liquid. The unstable coating adds to the cost and complexity of the processing. In this regard, it is timely to develop an affordable and scalable strategy that enables the attainment of robust photothermal ice-repellent surfaces, which can efficiently delay ice formation and remove ice in an on-demand manner.

Here, we report a facile strategy to fabricate the candle soot-based photothermal surface (PDMS/CS60@PDMS/Al) that can gain heat through the absorption of sunlight. The key factor is the construction of the photothermal layer with hierarchical micro/nanostructures, which relies on the deposition of candle soot nanoparticles. By adding a certain amount of adhesive (PDMS), our candle soot-based photothermal coating shows mechanical durability even after a 200 cm sandpaper abrasion test. The PDMS/CS60@PDMS/Al surface still remains at a high water contact angle (~148°) under the action of an external force (1 N). Benefiting from the hierarchical micro/nanostructures, the PDMS/CS60@PDMS/Al surface exhibits excellent photothermal performance (high absorbance of ~96%). The photothermal layer in our work can be widely applied to various substrates except aluminum, such as Cu, stainless steel, and glass slides, endowing it with great potential in practical applications. Moreover, by combining with superhydrophobicity, the photothermal performance of the surface endows the PDMS/CS60@PDMS/Al with the abilities of anti-icing and de-icing. By integrating sunlight illumination, the PDMS/CS60@PDMS/Al surface further exhibits self-cleaning performance.

2. Materials and Methods

2.1. Materials

Polydimethylsiloxane (PDMS) prepolymer (Sylgard 184) and the curing agent were provided from Dow Corning, Midland, MI, USA; n-Hexane was obtained from Aladdin

Biochemical Technology Co. Ltd., Shanghai, China; and the candle and polished aluminum (Al) sheets were purchased from the local market.

2.2. Fabrication of PDMS/Al Surface

The PDMS prepolymer and curing agent were first thoroughly mixed in a mass ratio of 10:1 and degassed in a vacuum chamber for 1 h. Then the PDMS solution was spin-coated onto the prepared Al substrate at 2000 rpm for 10 s. After the spin coating process, the sample was baked at 80 °C for 12 min to semi-harden the PDMS.

2.3. Fabrication of PDMS/Candle Soot@PDMS/Al (PDMS/CS@PDMS/Al) Surface

The PDMS/Al samples were first held above the flame of a candle to evenly deposit the candle soot (CS) layer. Subsequently, the mixed PDMS-n-hexene solution (PDMS: curing agent: n-hexene = 10:1:100) was sprayed onto the samples. After that, the samples were baked at 80 °C for 120 min to harden the PDMS. In this work, four sets of surfaces were fabricated by tuning the deposition time of CS for 10 s, 30 s, 60 s, and 120 s, respectively, which were denoted as PDMS/CS10@PDMS/Al, PDMS/CS30@PDMS/Al, PDMS/CS60@PDMS/Al, and PDMS/CS120@PDMS/Al, respectively.

2.4. Characterization of the PDMS/CS@PDMS/Al Surface

The surface morphologies of the PDMS/CS@PDMS/Al samples were observed by a field emission scanning electron microscope (FEI Scio 2 HiVac) with a low vacuum mode and an accelerating voltage of 5 kV. The amounts of C, O, and Si in the PDMS/CS@PDMS/Al samples were confirmed by using element dispersive spectroscopy. The variations of C 1s, O 1s, and Si 2p bonds of the PDMS/CS60@PDMS/Al surface were confirmed by using an X-ray photoelectron spectrometer (XPS) with an Al Kα X-ray source (Thermo Scientific K-Alpha, Waltham, MA, USA, spot size ~400 μm^2). The chemical compositions of the PDMS/CS60@PDMS/Al surface were examined by using a Fourier transform infrared spectrophotometer (FTIR, Nicolet 6700, Waltham, MA, USA). The absorbance in UV-Vis spectra of PDMS/CS@PDMS/Al samples was measured by using a spectrophotometer (UV-3600i Plus, Shimadzu, Long Beach, CA, USA). The relative thermal images of PDMS/CS@PDMS/Al samples were photographed by using an infrared thermal camera (A615, FLIR Systems, Wilsonville, OR, USA). Additionally, the static water contact angle and rolling angle of PDMS/CS@PDMS/Al samples were calculated with a Ramé-Hart goniometer (model 290-U1, Succasunna, NJ, USA). Droplets of ~5 μL volume were gently deposited on the samples, and the contact angles were measured using the optical fiber goniometer. The mechanical stability is tested by using sandpaper abrasion. Firstly, 300-mesh sandpaper was used and fixed to the table. The PDMS/CS60@PDMS/Al surface was placed on the sandpaper. Then, a 100 g weight was pressed on the sample to provide the applied pressure. The PDMS/CS60@PDMS/Al surface was pulled on the sandpaper surface at different distances. The mechanical stability was characterized by the contact angle on the PDMS/CS60@PDMS/Al surface. The contact angle values were measured at every 20 cm distance. To ensure the repeatability of the results, all measurements were repeated at least three times.

2.5. Visualization of Droplet De-Icing and Anti-Icing Processes on the PDMS/CS60@PDMS/Al Surface

The droplet freezing experiment on the PDMS/CS60@PDMS/Al surfaces was carried out in a seal chamber. The relative humidity of the sealed chamber was maintained at 5% by filling in dry nitrogen and recorded by a humidity sensor (Testo 605i, Thermo-Hygrometer Smart Probe, Titisee-Neustadt, Germany). The low value of the relative humidity avoided the processes of condensation and frost formation. Initially, the samples were horizontally placed on the cooling stage (Cole-Parmer Standard Benchtop Chilling Block, Vernon Hills, IL, USA) with a preset temperature of −15 °C, −20 °C, and −25 °C, respectively. Then, a 10 μL droplet was deposited on the samples. The illumination of sunlight is carried out

by using a solar simulator. The droplet freezing process under 1-sun illumination was recorded by using two CCD cameras at 500 frames per second from the side view (EO-5032M, Navitar Zoom 6000, Burnsville, MN, USA) and the top view (WP-UT530M, Work Power, Shenzhen, CN). The de-icing process of the PDMS/CS60@PDMS/Al surface was carried out under one sunlight illustration and recorded by using the CCD camera from the top view (WP-UT530M, Work Power, Shenzhen, CN). The freezing statistics experiment was carried out in a sealed chamber with 5% relative humidity. The samples were horizontally placed on the cooling stage (Cole-Parmer Standard Benchtop Chilling Block) with a preset temperature of −15 °C. Then, with the illumination of 1-sun, the freezing dynamics of ~100 water droplets with a volume of 5 μL on the cooled bare Al surface (−15 °C) and on the cooled PDMS/CS60@PDMS/Al surface (−15 °C) were analyzed. The freezing delay time is defined as the time interval when the transparency of the frozen droplet changes from clear to opaque. The experiment was recorded by a CCD camera at 500 frames per second from the top view (WP-UT530M, Work Power). To ensure the repeatability of the results, all experiments were repeated at least three times.

3. Results

3.1. Fabrication and Characterization of PDMS/CS60@PDMS/Al

We constructed polydimethylsiloxane/candle soot60@polydimethylsiloxane/Aluminum (PDMS/CS60@PDMS/Al) based on the deposition of candle soot (CS) onto a PDMS/Al surface, where the photothermal performance of the CS layer can be tailored by controlling the deposition time. The PDMS/CS60@PDMS/Al was made through combined spin-coating and vapor deposition technology. (Figure 1a). Briefly, to strengthen the CS layer and make the coating robust, a PDMS layer was first prepared by spin-coating the pure PDMS solution onto the Al surface (PDMS/Al) at 2000 rpm for 10 s. The PDMS/Al surface was then baked at 80 °C for 12 min to semi-harden the PDMS layer. After that, CS nanoparticles were facilely deposited evenly onto the PDMS/Al surface by holding it above the flame of a candle for 60 s. To induce low surface energy, a mixed PDMS/n-hexene solution was sprayed onto the CS layer, and the sample was baked at 80 °C for 120 min. This three-layer surface, consisting of the underlying supporting PDMS layer, the middle photothermal CS layer, and the upper superhydrophobic PDMS layer, is termed the PDMS/CS60@PDMS/Al. For comparison, we also fabricated three sets of surfaces by governing the deposition time of CS nanoparticles within 10 s, 30 s, and 120 s, which were denoted as PDMS/CS10@PDMS/Al, PDMS/CS30@PDMS/Al, and PDMS/CS120@PDMS/Al, respectively. It should be noted that the photothermal CS layer in our work can be applied to some other substrates except aluminum. We can fabricate the photothermal CS layer on substrates such as Cu, stainless steel, and glass slides. There is only one condition the substrates should meet, namely, that they can be resistant to the high temperature of the flame of a candle (500 °C). Therefore, the photothermal layer in our work can be widely applied to various substrates, indicating great practical significance in many fields.

Figure 1b–e show the scanning electron microscopy (FEI Scios) images of PDMS/CS10@PDMS/Al, PDMS/CS30@PDMS/Al, PDMS/CS60@PDMS/Al, and PDMS/CS120@PDMS/Al, respectively. Owing to the incomplete combustion of candle flame [32–34]. CS nanoparticles are generated to form the CS layer on the as-fabricated surfaces. The interconnected CS nanoparticles have a diameter of 200 nm. With a 10 s deposition time, CS nanoparticles are seldom generated on the PDMS/CS10@PDMS/Al (Figure 1b). The amount of CS nanoparticles on the CS layer increases with the deposition time. After being deposited on the candle flame for 30 s and 60 s, the morphologies of CS layers show homogeneous micro-porous structures, which consist of increased CS nanoparticles (Figures 1c and 1d). These hierarchical micro/nanostructures of CS layers on the PDMS/CS30@PDMS/Al and the PDMS/CS60@PDMS/Al surfaces significantly enhance the surface roughness. However, when the deposition time is 120 s, too many CS nanoparticles agglomerate to form the CS layer (Figure 1e). Due to the weak physical inter-

actions between CS nanoparticles, the CS layer on the PDMS/CS120@PDMS/Al is too loose to form a strong bond with the underlying PDMS layer. Figure 1f,g show the cross-section micrographs of the PDMS/CS30@PDMS/Al surface and the PDMS/CS120@PDMS/Al, respectively. It can be seen that the thickness of the candle soot photothermal layer of the PDMS/CS30@PDMS/Al surface is smaller than that of the PDMS/CS120@PDMS/Al surface. Figure 1h shows the C mapping in the cross section of the PDMS/CS120@PDMS/Al surface. The PDMS/CS@PDMS/Al is further characterized by element dispersive spectroscopy (EDS) analysis according to the mapping in cross-section micrographs. It can be seen that the PDMS/CS30@PDMS/Al contains 63.5% of C, 22.5% of Si, and 14.0% of O (Figure 1i). The amount of C confirms the formation of the CS nanoparticles, while the amount of Si and O 1s indicates the existence of the PDMS layer. Furthermore, the content of C rises from 50.5% to 84.9% when the deposited time increases from 10 s to 120 s. The dramatic increase in C content is due to the fact that the main content of soot is branched saturated hydrocarbons. Furthermore, when the deposited time is 10 s, the content of the Si element is 31.8%. When the deposited time is 60 s, the content of Si decreases to 10.0%. The decrease in Si content is owing to the decomposition of PDMS during the deposition process.

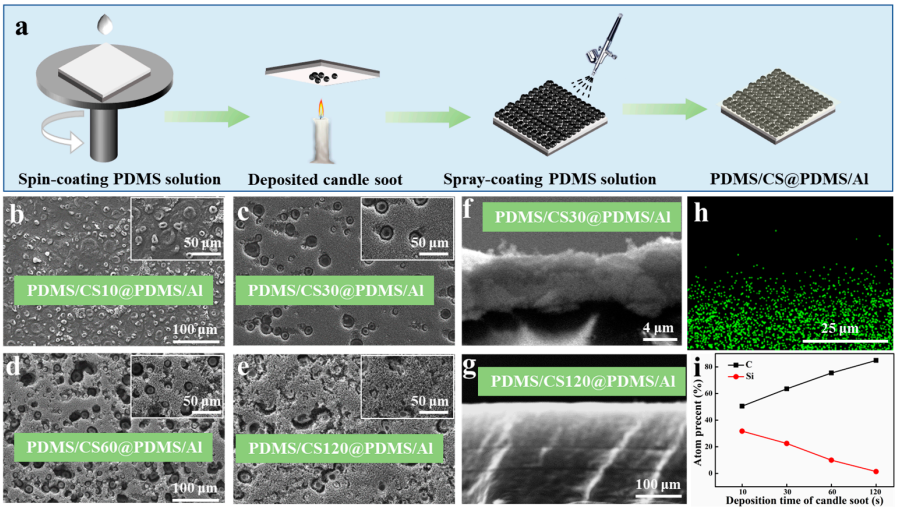

Figure 1. Fabrication and characterization of PDMS/CS60@PDMS/Al. (**a**) Schematic drawing of the fabrication process of the PDMS/CS@PDMS/Al surface. FEI Scios images of (**b**) PDMS/CS10@PDMS/Al, (**c**) PDMS/CS30@PDMS/Al, (**d**) PDMS/CS60@PDMS/Al, and (**e**) PDMS/CS120@PDMS/Al, respectively. Cross-section micrographs for (**f**) PDMS/CS30@PDMS/Al and (**g**) PDMS/CS120@PDMS/Al surfaces. (**h**) EDS analysis of the PDMS/CS60@PDMS/Al. (**i**) The amount of C and Si for the surfaces with different deposited times.

Figure 2a shows the high-resolution XPS spectra of the Si 2p peak for the PDMS/CS60@PDMS/Al surface. The Si 2p peak can be deconvoluted into an organic Si peak at 102.3 eV and a SiO_2 peak at 103.4 eV [35]. This result proves that PDMS is decomposed during the candle soot deposition process, and part of organic Si is transformed into SiO_2. Furthermore, Figure 2a exhibits the FTIR spectrum of the PDMS/CS60@PDMS/Al surface. There are four peaks in the infrared spectrum that indicate the presence of a CH_3 group, namely, 2953 cm^{-1} (stretching vibration), 1249 cm^{-1} (in-plate bending vibration), 997 cm^{-1} (out-of-plate bending vibration), and 774 cm^{-1} (out-of-plate bending vibration). In combination with the XPS spectrum, it can be deduced that there is a physical interaction between the PDMS layer and the aluminum surface and a chemical interaction between the PDMS layer and the candle soot layer. The PDMS layer and the candle soot layer were successfully fixed on the PDMS/CS60@PDMS/Al surface. The static water contact angle and the rolling angle of the as-fabricated surfaces are shown in Figure 2c. The PDMS/CS10@PDMS/Al shows a static water contact angle of ~123° and a rolling angle

of ~14°, due to the lack of enough CS nanoparticles to form the micro/nanostructure of the CS layer on the surface. When the deposition time is greater than 30 s, the hierarchical micro/nanostructure of the CS layers endows the surfaces with superhydrophobicity. The surface roughness of the as-fabricated PDMS/CS@PDMS/Al is ~6 μm [36–38]. Notably, the PDMS/CS60@PDMS/Al exhibits the largest water contact angle (~163°) and the smallest rolling angle (~1°). The mechanical stability of a superhydrophobic surface is important for practical application [39]. Figure 2d shows the PDMS/CS60@PDMS/Al surface was pulled on the sandpaper surface under 1 N. At the initial moment, the contact angle of the PDMS/CS60@PDMS/Al surface is ~163°. When the PDMS/CS60@PDMS/Al surface was pulled on the sandpaper surface for 100 cm, the contact angle was ~152°. Obviously, even after the 200 cm sandpaper abrasion test, the PDMS/CS60@PDMS/Al surface still remains at a high water contact angle (~148°). Therefore, the PDMS/CS60@PDMS/Al surface possesses mechanical durability under the action of external force.

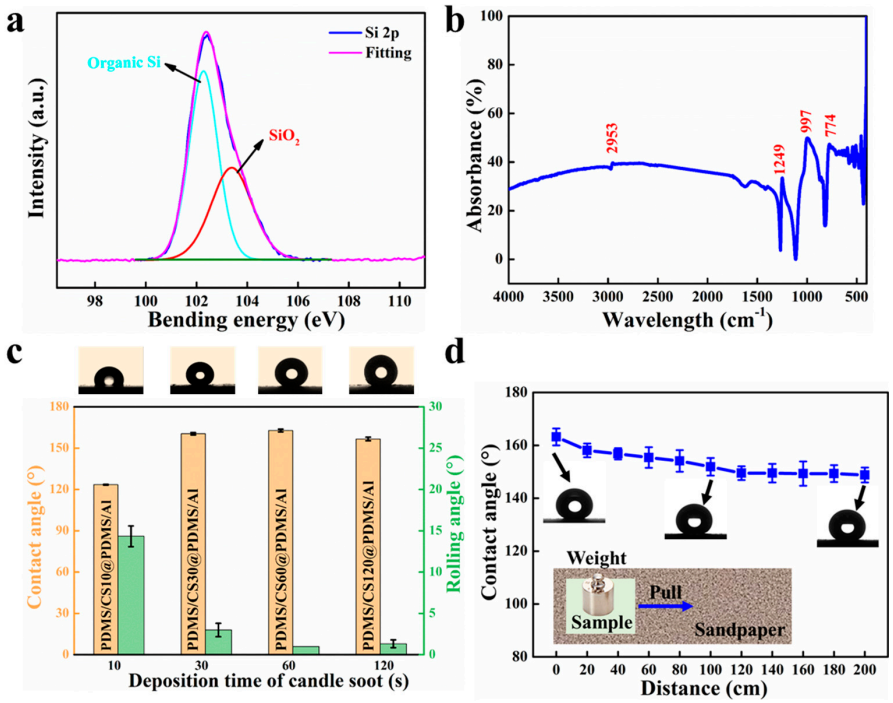

Figure 2. Characterization of PDMS/CS60@PDMS/Al. (**a**) High-resolution XPS spectra of the Si 2p peak for the PDMS/CS60@PDMS/Al surface. (**b**) FTIR spectrum of the PDMS/CS60@PDMS/Al surface. (**c**) The static contact angle and rolling angle of the PDMS/CS10@PDMS/Al, PDMS/CS30@PDMS/Al, PDMS/CS60@PDMS/Al, and PDMS/CS120@PDMS/Al surfaces. (**d**) Mechanical stability test of the PDMS/CS60@PDMS/Al surface.

3.2. Photothermal Performance of PDMS/CS60@PDMS/Al

To examine whether the PDMS/CS60@PDMS/Al can achieve a sufficiently large heat to delay the freezing of water droplets by raising the surface temperature, we first investigate the photothermal performance of the PDMS/CS60@PDMS/Al under sunlight illumination. Figure 3a shows the absorbance of the PDMS/CS10@PDMS/Al, PDMS/CS30@PDMS/Al, PDMS/CS60@PDMS/Al, and PDMS/CS120@PDMS/Al, respectively. Beneficial to the nanoscale CS particles, the hierarchical micro/nanostructure of the CS layer can effectively trap and absorb light [40]. The absorbance of all the samples is approaching 96% throughout the visible and near-infrared light ranges. This remarkable absorption further improves the photothermal performance of the surfaces.

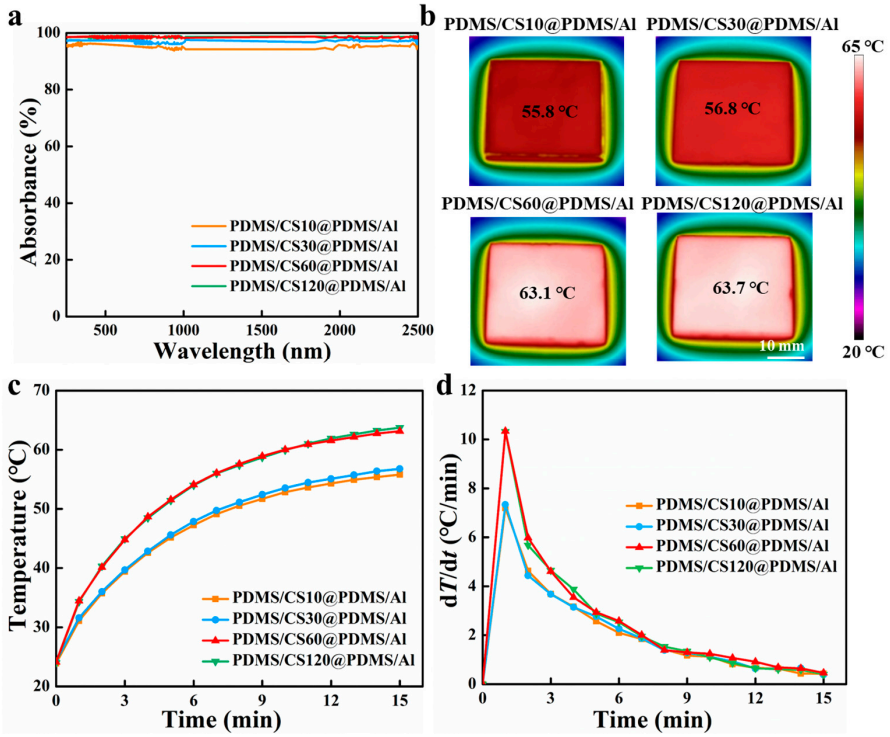

Figure 3. Photothermal performance of PDMS/CS60@PDMS/Al. (**a**) The absorbance of the as-fabricated PDMS/CS@PDMS/Al surfaces throughout the visible and near-infrared light ranges. (**b**) Infrared images of the as-fabricated PDMS/CS@PDMS/Al surfaces at 15 min under 1-sun illumination. (**c**) Time-dependent temperature profile and (**d**) temperature-changing rate (dT/dt) of the irradiated area on the as-prepared PDMS/CS@PDMS/Al surfaces with 1-sun illumination.

The photothermal performance is then investigated based on the variation of surface temperature under 1-sun illumination (1 kW/m^2). As is depicted in the infrared images in Figure 3b, the surface temperature sharply increases with the sunlight illumination time, which is sensitive to the deposition time of CS nanoparticles. The longer the deposition time is, the more obvious the temperature rise of the surfaces under sunlight illumination. Within 15 min illumination of 1-sun, the surface temperature of PDMS/CS10@PDMS/Al increases from 24.0 °C to 55.8 °C, whereas the surface temperature of PDMS/CS60@PDMS/Al increases from 24.0 °C to 63.1 °C (Figure 3c). Meanwhile, the maximum temperature rising rate (dT/dt) on the PDMS/CS60@PDMS/Al surface can reach ~10.3 °C/s (Figure 3d). This remarkable dT/dt on the PDMS/CS60@PDMS/Al is significantly higher than that on the other as-prepared surfaces, indicating superior photothermal performance (PDMS/CS60@PDMS/Al is used in the following section).

3.3. Anti-Icing Performance of PDMS/CS60@PDMS/Al

Due to the excellent photothermal property of the PDMS/CS60@PDMS/Al, anti-icing can be achieved on the surface under sunlight illumination. To evaluate the anti-icing performance of the PDMS/CS60@PDMS/Al, we investigated the freezing dynamics of the water droplet (10 μL) on the cooled surface with sunlight illumination. As shown in Figure 4a, when a water droplet is deposited on the cooled bare Al surface (−15 °C) under 1-sun illumination, the droplet exhibits a hemispherical shape at 0 s (Video S1, Supplementary Materials). After 6 s, the droplet transforms from a transparent state to a non-transparent state and starts to freeze. The freezing front propagates from the bottom to the top until the droplet is completely frozen with a peach-tip shape at 26 s [41,42].

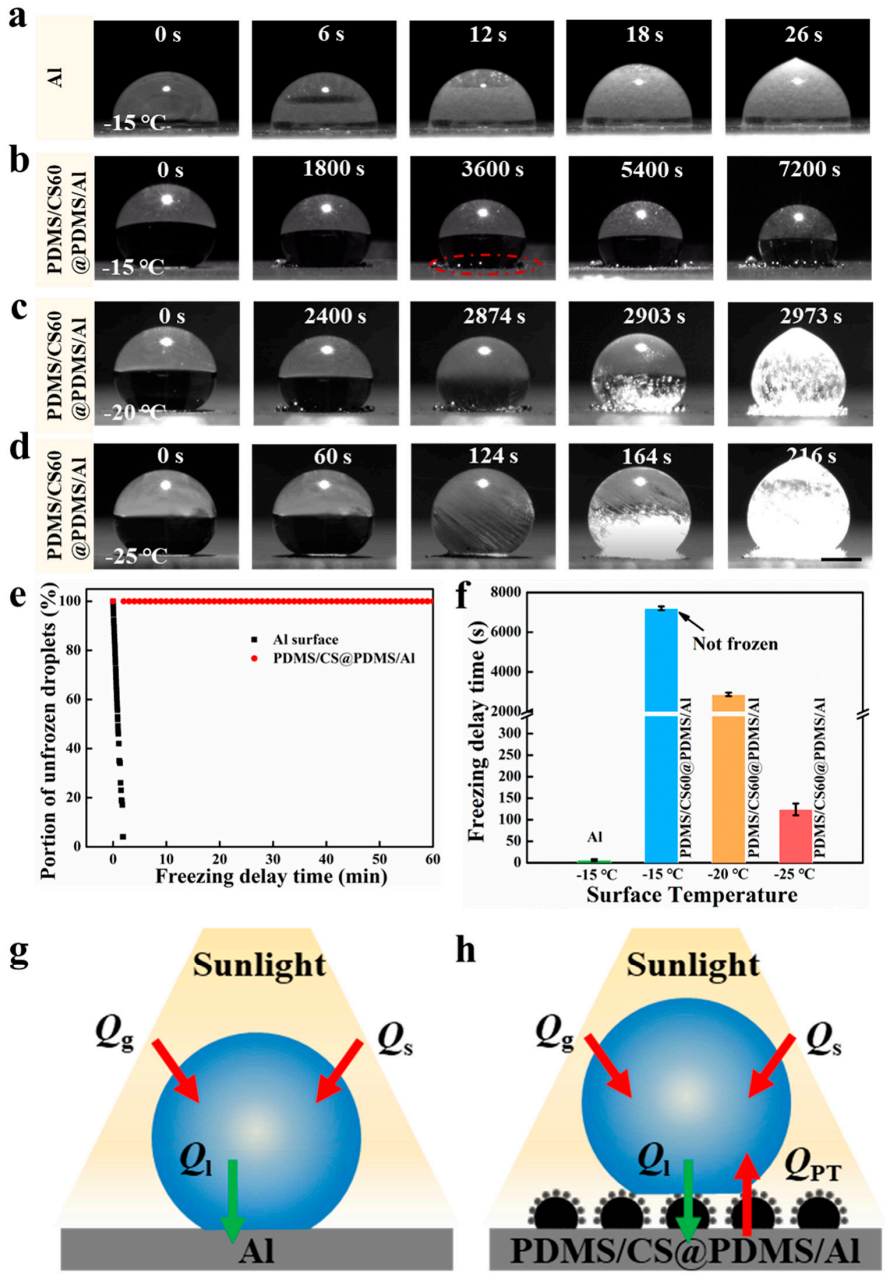

Figure 4. Anti-icing performance of PDMS/CS60@PDMS/Al with different surface temperatures. (**a**) Freezing process of a water droplet (10 μL) on the cooled bare Al surface (−15 °C) under 1-sun illumination. (**b**) Freezing process of a water droplet (10 μL) on the cooled PDMS/CS60@PDMS/Al surface (−15 °C) under 1-sun illumination (multi tiny droplets is circled by red dashed circles). (**c**) Freezing process of a water droplet (10 μL) on the cooled PDMS/CS60@PDMS/Al surface (−20 °C) under 1-sun illumination. (**d**) Freezing process of a water droplet (10 μL) on the cooled PDMS/CS60@PDMS/Al surface (−25 °C) under 1-sun illumination. (**e**) Relation between portion of unfrozen droplets and freezing delay time on the cooled bare Al surface (−15 °C) and on the cooled PDMS/CS60@PDMS/Al surface (−15 °C) under 1-sun illumination. (**f**) Freezing delay time of the Al and the as-fabricated PDMS/CS@PDMS/Al surfaces. Heat transfer model between the droplet and the cooled (**g**) bare Al surface and (**h**) PDMS/CS@PDMS/Al surface with sunlight illumination. Scale bar: 1 mm.

However, on the cooled PDMS/CS60@PDMS/Al surface (−15 °C), the droplet is spherical at the initial state (Figure 4b). Under 1-sun illumination, the droplet stays in a transpar-

ent state and does not freeze even after 7200 s. It confirms that the freezing of the droplet can be greatly delayed on the PDMS/CS60@PDMS/Al with the sunlight illumination. This freezing delay phenomenon is ascribed to two factors: one is the small contact area, and the other is the superior photothermal performance of the PDMS/CS60@PDMS/Al. The small contact area, which relies on the hierarchical micro/nanostructures of the CS layer, leads to a decrease in the heat conduction path between the droplet and the PDMS/CS60@PDMS/Al surface. Moreover, under 1-sun illumination, the favorable photothermal property of the surface enables the CS layer to continuously obtain more heat, which thus prolongs the freezing time. Notably, the volume of the droplet is reducing with time under 1-sun illumination. This is because droplet evaporation happens. After being illuminated by 1-sun, the PDMS/CS60@PDMS/Al surface gains huge heat transformed from sunlight due to its superior photothermal property. And the surface temperature of PDMS/CS60@PDMS/Al is rising. Therefore, the droplet deposited on the cooled PDMS/CS60@PDMS/Al surface (−15 °C) experiences a temperature rise. After 7200 s, the volume of the droplet is smaller than the volume of the droplet at the initial moment (0 s). Furthermore, the droplet evaporation is accompanied by multiple tiny droplets forming on the solid-liquid-vapor three-phase contact line. The formation of multiple tiny droplets is due to the fact that there is a supersaturation pressure of water vapor on the solid-liquid-vapor three-phase contact line [43,44]. Under sunlight illumination, these multiple tiny droplets don't evaporate due to their small contact area on the surface and develop a ring pattern surrounding the deposited droplet (circled by red dashed circles). Further cooling the PDMS/CS60@PDMS/Al surface to −20 °C (Figure 4c), there also exists a tiny droplet ring pattern under 1-sun illumination (Video S2, Supplementary Materials). The droplet completely freezes after 2973 s. When the surface temperature of the PDMS/CS60@PDMS/Al decreases to −25 °C (Figure 4d), the droplet appears to be opaque at 124 s and freezes at 216 s with 1-sun illumination.

The freezing dynamics are characterized by using the freezing delay time, which is defined as the time interval when the transparency of the frozen droplet changes from clear to opaque. Figure 4e shows statistics of droplets freezing on the cooled Al surface (−15 °C) and on the cooled PDMS/CS60@PDMS/Al surface (−15 °C) under 1-sun illumination. As is depicted, all of the water droplets on the cooled Al surface freeze within 5 min, whereas the majority of water droplets on the cooled PDMS/CS60@PDMS/Al surface show a remarkable freezing delay of 1 h. This is because of the superior photothermal performance of the PDMS/CS60@PDMS/Al surface. As for the single droplet on the surface (Figure 4f), the freezing delay time on the cooled Al and the PDMS/CS60@PDMS/Al (−15 °C) under 1-sun illumination is ~ 6 s and ~ 7200 s. The freezing delay time decreases with the reduction in surface temperature. Remarkably, with a lower surface temperature of −25 °C, freezing delay can still happen on the cooled PDMS/CS60@PDMS/Al under 1-sun illumination, indicating the anti-performance of the PDMS/CS60@PDMS/Al. Furthermore, we compared the anti-icing performance between our work and the previous reports (Table 1). It can be seen that the water droplet freezing delay time is larger than that in the literature, indicating a superior anti-icing performance of the PDMS/CS60@PDMS/Al in our work.

Table 1. Comparison of anti-icing performance between the PDMS/CS60@PDMS/Al surface in this work and as-fabricated surfaces in the literatures.

Surfaces	Freezing Delay Time (s)	Reference
PDMS/CS60@PDMS/Al in this work	7200	This work
Bio-inspired micro-structure surface	1938	[1]
Nanostructured surface	1740	[15]
MWCNT based photothermal surface	1800	[45]
Cuttlefish juice based photothermal surface	144	[46]

3.4. Mechanism of Anti-Icing Permance of PDMS/CS60@PDMS/Al

We then explore the underlying mechanism of anti-icing performance by establishing the heat transfer model between the droplet and the cooled PDMS/CS@PDMS/Al surface with sunlight illumination. As is shown in Figure 4g, the droplet on the cooled surface is considered a comprehensive solid-liquid-vapor three-phase system. When the droplet is deposited on the cooled Al surface with sunlight illumination, it gains heat from the air through heat conduction and heat radiation; it also obtains heat from sunlight; and it loses heat to the cooled Al surface through heat conduction and heat irradiation. The net heat gain of the droplet on the bare Al surface in unit time under sunlight illumination can be expressed as:

$$\Delta Q = Q_g + Q_s - Q_l \quad (1)$$

where ΔQ is the net heat gain of the droplet in unit time on the bare Al surface, Q_g is the heat gain of the droplet in unit time from the air, Q_s is the heat gain of the droplet in unit time from sunlight, and Q_l is the heat loss of the droplet in unit time to the cooled Al surface, respectively. Obviously, the droplet on the bare Al surface undergoes a fast-freezing process within 26 s (Figure 4a), indicating a small ΔQ of the droplet even after being illuminated by sunlight. As for the PDMS/CS60@PDMS/Al surface under sunlight illumination (Figure 4f), the droplet also gains heat from the photothermal surface in the form of heat conduction and heat radiation. The net heat gain of the droplet in unit time on the PDMS/CS60@PDMS/Al surface under sunlight illumination can be expressed as:

$$\Delta Q = Q_g + Q_s + Q_{pt} - Q_l \quad (2)$$

where Q_{pt} is the heat gain of the droplet in unit time from the PDMS/CS60@PDMS/Al surface under sunlight illumination. Notably, the additional heat transfer from the photothermal surface to the droplet leads to a large Q_{pt}, so the ΔQ of the droplet on the cooled PDMS/CS60@PDMS/Al surface is far larger than that of the droplet on the cooled bare Al surface. Moreover, the decreased temperature of the droplet in unit time during the freezing process can be expressed as:

$$\Delta T = \frac{\rho_w C_p (T_w - T_S)}{\Delta Q} \quad (3)$$

where ΔT is the decreased temperature of the water droplet, ρ_w is the water density, C_p is the heat capacity of water at constant pressure, T_w is the initial temperature of the water droplet, and T_s is the temperature of the cooled surface, respectively. It can be deduced that a smaller ΔT can be induced by a larger value of ΔQ, which results in a longer freezing delay time eventually.

Compared with that on the cooled bare Al surface (Figure 4f), a larger freezing delay time was observed on the cooled PDMS/CS60@PDMS/Al surface under the same experimental conditions. It reflects that the PDMS/CS60@PDMS/Al has superior photothermal performance and anti-icing ability. The mechanism of prolonged freezing delay on the cooled PDMS/CS60@PDMS/Al surface is further discussed in detail. The main reason for the prolonged freezing delay on the PDMS/CS60@PDMS/Al surface is related to the high energetic barrier and time lag for heterogeneous nucleation in the sessile droplet. According to the theory of nucleation kinetics [47], heterogeneous nucleation plays a major role in icing delay. The relation between the portion of unfrozen sessile droplets on the substrate is proportional to the area available for heterogeneous nucleation. This area between the sessile droplet and the surface is defined by the contact angle and the portion of wetted area. In terms of the PDMS/CS60@PDMS/Al surface, because of the higher apparent contact angle, the portion of wetted area is much less than for the bare Al surface. Moreover, the PDMS/CS60@PDMS/Al surface has a high energy barrier for heterogeneous nucleation. Thus, the freezing delay for the PDMS/CS60@PDMS/Al surface is larger than that for the bare Al surface.

The anti-icing property is further demonstrated by analyzing the freezing behaviors of droplets (10 μL) with various values of PH on the PDMS/CS60@PDMS/Al surface at −15 °C under 1-sun illumination. As is shown in Figure 5a–c, an HCl droplet (PH = 1), a NaCl droplet (PH = 7), and a NaOH droplet (PH = 14) are deposited on the cooled PDMS/CS60@PDMS/Al surface, respectively. With 1-sun illumination, all of the droplets are spherical at the initial state, indicating that the contact areas of the droplets with different PH values are all small enough to hinder the heat transfer from the droplets to the cooled PDMS/CS60@PDMS/Al surface. Due to the temporary increase of the surface temperature under sunlight illumination, flash evaporation happens on the HCl droplet, the NaCl droplet, and the NaOH droplet. Among them, the HCl droplet shows the fastest evaporation rate and is surrounded by a ring pattern (circled by red dashed circles). This fast evaporation of the HCl droplet is attributed to the existence of a large supersaturation gas pressure, which is triggered by the easily volatilized HCl molecular weight (Figure 5a). Meanwhile, some white NaCl crystals form when the NaCl droplet vaporizes (Figure 5b). The formation of the NaCl crystals may be due to the fact that there is a circular flow inside the NaCl droplet caused by the Marangoni effect [48,49]. Under sunlight illumination, the Marangoni flow carries the NaCl particles with it and accumulates them on the bottom of the NaCl droplet. When the surface is illuminated by sunlight after 7200 s, all of the droplets with different PH values are not frozen on the PDMS/CS60@PDMS/Al surface (Figure 5c).

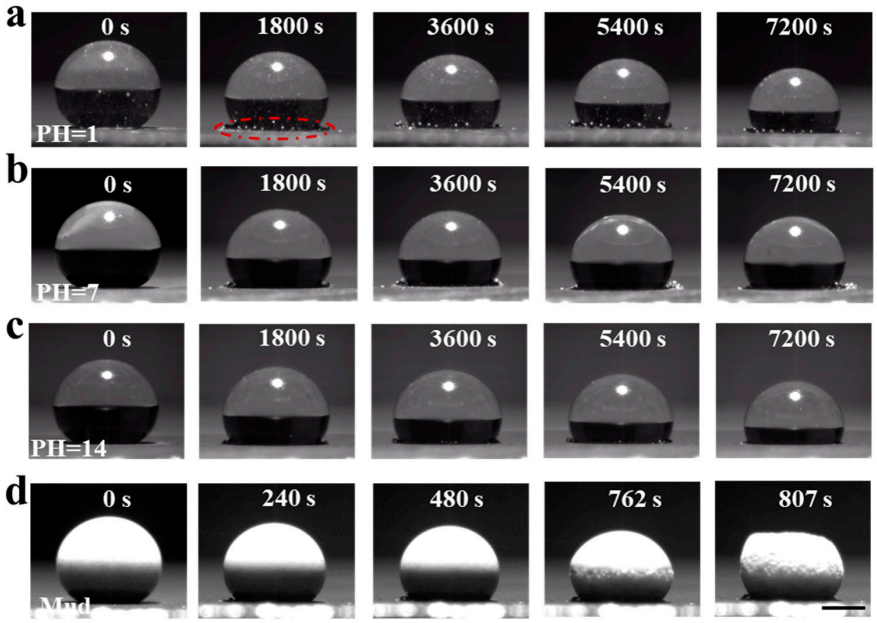

Figure 5. Anti-icing performance of PDMS/CS60@PDMS/Al in terms of droplets with different PH values. Freezing process of (**a**) an HCl droplet (PH = 1, multi tiny droplets is circled by red dashed circles), (**b**) a NaCl droplet (PH = 7), and (**c**) a NaOH droplet (PH = 14) on the cooled PDMS/CS60@PDMS/Al surface (−15 °C) under 1-sun illumination, respectively. (**d**) Freezing process of a mud droplet (10 μL) on the cooled PDMS/CS60@PDMS/Al surface (−15 °C) under 1-sun illumination. Scale bar: 1 mm.

In addition, in terms of a mud droplet freezing on a cooled PDMS/CS60@PDMS/Al surface (−15 °C) under 1-sun illumination (Figure 5d), the freezing process can be accelerated by two factors [50]. The first is the inherent non-transparent state of the mud droplet, which strongly lessens the photothermal performance due to the fact that sunlight cannot pass through the mud droplet to the surface. The second is the existence of undesirable ice nucleation sites in the mud droplet, which are generated from the mud particles and can further speed up the mud droplet freezing process. Nevertheless, the mud droplet on

the cooled PDMS/CS60@PDMS/Al surface still shows a freezing delay phenomenon with 1-sun illumination. The mud droplet does not completely freeze before ~807 s. Furthermore, there is an annular flow on the top side of the mud droplet due to the Marangoni effect. Therefore, the mud droplet forms a flat pattern when it is completely frozen. The above-mentioned results prove that our PDMS/CS60@PDMS/Al can not only be applied to anti-icing with different surface-cooled temperatures but also to practical anti-icing for droplets with various values of PH as well as for droplets in the mud environment.

3.5. De-Icing Performance and Self-Cleaning Performance of PDMS/CS60@PDMS/Al

De-icing can also be realized on the PDMS/CS60@PDMS/Al under sunlight illumination. As depicted in Figure 6a,b, an ice layer with a thickness of 4 mm was allowed to accumulate on the cooled bare Al surface and the cooled PDMS/CS60@PDMS/Al surface (−15 °C) in advance, respectively. After being illuminated by 1-sun for 1710 s, the ice layer on the cooled bare Al surface does not melt. By contrast, with the same illumination time of 1-sun, the ice layer on the cooled PDMS/CS60@PDMS/Al surface completely melts. Note that the rolling angle of the PDMS/CS60@PDMS/Al surface is ~1°. Most of the melted water droplets can roll off the surface. The outstanding ice-repellency of the surface is attributed to the synergistic cooperation of the excellent photothermal performance and the superior superhydrophobicity. Furthermore, the PDMS/CS60@PDMS/Al also shows a self-cleaning feature. As shown in Figure 6c, the cooled PDMS/CS60@PDMS/Al surface (−15 °C) was first covered by opaque contaminants (Al_2O_3 powders). The contaminants can be easily removed by continually injecting water flow to the surface. The injected water droplets do not freeze and can easily slide away with 1-sun illumination. It reflects that the PDMS/CS60@PDMS/Al possesses the self-cleaning ability to avoid the contaminants covering the surface and to guarantee outstanding photothermal performance.

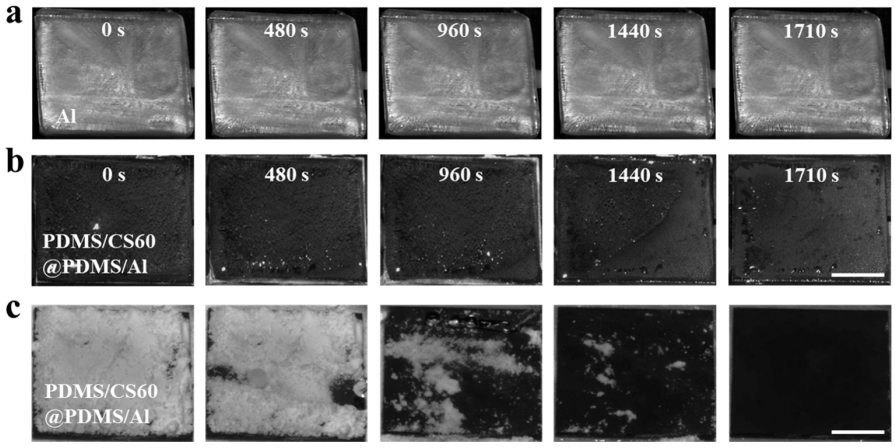

Figure 6. De-icing and self-cleaning performance of PDMS/CS60@PDMS/Al. An ice layer (thickness ~4 mm) melting process on (**a**) the cooled bare Al and (**b**) the cooled PDMS/CS60@PDMS/Al surface (−15 °C), respectively. (**c**) Contaminants on the cooled PDMS/CS60@PDMS/Al surface (−15 °C) are removed by injecting water flow under 1-sun illumination. Scale bar: 10 mm.

4. Conclusions

In summary, we develop a novel candle soot-based superhydrophobic surface (PDMS/CS60@PDMS/Al) for photothermal anti-icing and de-icing. The hierarchical micro/nanostructures of the as-fabricated PDMS/CS60@PDMS/Al endow the surface with high absorbance (~96%) throughout the visible and near-infrared light range. Under 1-sun sunlight illumination, the surface temperature rises from 24.0 °C to 63.1 °C within 15 min, and the maximum temperature rising rate (dT/dt) on the PDMS/CS60@PDMS/Al surface can reach ~10.3 °C/s, indicating a superior photothermal performance. Such a large temperature rising rate (dT/dt) of the PDMS/CS60@PDMS/Al makes it easier to delay freezing for droplets with various values of PH or droplets in the mud environment. The

freezing delay time can be prolonged to ~ 7200 s to hold back the ice formation at a subzero surface temperature of −15 °C with 1-sun illumination. The underlying mechanism is elucidated by establishing the heat transfer model between the droplets and the cooled surface. Furthermore, benefiting from the superhydrophobicity and excellent photothermal performance, after being illuminated by sunlight, the PDMS/CS60@PDMS/Al surface can achieve rapid melting of the interface ice layers, inducing the multi-abilities of de-icing and self-cleaning. We envision that this work could open a new avenue for the development of novel photothermal surfaces to enhance anti-icing, anti-frosting, and de-icing abilities for practical applications in subzero temperature environments.

Supplementary Materials: The following supporting information can be downloaded at: https://www.mdpi.com/article/10.3390/coatings14050612/s1, Video S1: Freezing process of a water droplet on the cooled Al surface (−15 °C) under 1-sun illumination; Video S2: Freezing process of a water droplet on the cooled PDMS/CS60@PDMS/Al surface (−20 °C) with 1-sun illumination.

Author Contributions: Conceptualization, X.C.; methodology, X.C., C.Q. and L.W.; validation, C.Q. and L.W.; formal analysis, C.Q., L.W. and X.C.; writing—original draft preparation, C.Q., L.W. and X.C.; writing—review and editing, X.C. and Q.L.; supervision, X.C. and Q.L; project administration, X.C. and Q.L.; All authors have read and agreed to the published version of the manuscript.

Funding: This research was funded by the National Natural Science Foundation of China (52276071 and U2241252).

Institutional Review Board Statement: Not applicable.

Informed Consent Statement: Not applicable.

Data Availability Statement: Data are contained within the article.

Conflicts of Interest: The authors declare no conflicts of interest.

References

1. Liu, Y.; Li, X.; Jin, J.; Liu, J.; Yan, Y.; Han, Z.; Ren, L. Anti-Icing Property of Bio-Inspired Micro-Structure Superhydrophobic Surfaces and Heat Transfer Model. *Appl. Surf. Sci.* **2017**, *400*, 498–505. [CrossRef]
2. Zhang, H.; Jin, Z.; Jiao, M.; Yang, Z. Experimental Investigation of the Impact and Freezing Processes of a Water Droplet on Different Cold Concave Surfaces. *Int. J. Therm. Sci.* **2018**, *132*, 498–508. [CrossRef]
3. Gao, L.; Liu, Y.; Hu, H. An Experimental Investigation of Dynamic Ice Accretion Process on a Wind Turbine Airfoil Model Considering Various Icing Conditions. *Int. J. Heat Mass Transf.* **2019**, *133*, 930–939. [CrossRef]
4. Yirtici, O.; Ozgen, S.; Tuncer, I.H. Predictions of Ice Formations on Wind Turbine Blades and Power Production Losses Due to Icing. *Wind Energy* **2019**, *22*, 945–958. [CrossRef]
5. Zhao, Z.; Chen, H.; Zhu, Y.; Liu, X.; Wang, Z.; Chen, J. A Robust Superhydrophobic Anti-Icing/de-Icing Composite Coating with Electrothermal and Auxiliary Photothermal Performances. *Compos. Sci. Technol.* **2022**, *227*, 109578. [CrossRef]
6. Rashid, T.; Khawaja, H.A.; Edvardsen, K. Review of Marine Icing and Anti-/de-Icing Systems. *J. Mar. Eng. Technol.* **2016**, *15*, 79–87. [CrossRef]
7. Wang, Y.; Xu, Y.; Huang, Q. Progress on Ultrasonic Guided Waves De-Icing Techniques in Improving Aviation Energy Efficiency. *Renew. Sustain. Energy Rev.* **2017**, *79*, 638–645. [CrossRef]
8. Wang, Y.; Xu, Y.; Su, F. Damage Accumulation Model of Ice Detach Behavior in Ultrasonic De-Icing Technology. *Renew. Energy* **2020**, *153*, 1396–1405. [CrossRef]
9. Ding, L.; Chang, S.; Yi, X.; Song, M. Coupled Thermo-Mechanical Analysis of Stresses Generated in Impact Ice during in-Flight de-Icing. *Appl. Therm. Eng.* **2020**, *181*, 115681. [CrossRef]
10. Shome, A.; Das, A.; Borbora, A.; Dhar, M.; Manna, U. Role of Chemistry in Bio-Inspired Liquid Wettability. *Chem. Soc. Rev.* **2022**, *51*, 5452–5497. [CrossRef]
11. Rykaczewski, K.; Anand, S.; Subramanyam, S.B.; Varanasi, K.K. Mechanism of Frost Formation on Lubricant-Impregnated Surfaces. *Langmuir* **2013**, *29*, 5230–5238. [CrossRef] [PubMed]
12. Stamatopoulos, C.; Hemrle, J.; Wang, D.; Poulikakos, D. Exceptional Anti-Icing Performance of Self-Impregnating Slippery Surfaces. *ACS Appl. Mater. Interfaces* **2017**, *9*, 10233–10242. [CrossRef] [PubMed]
13. Kreder, M.J.; Alvarenga, J.; Kim, P.; Aizenberg, J. Design of Anti-Icing Surfaces: Smooth, Textured or Slippery? *Nat. Rev. Mater.* **2016**, *1*, 15003. [CrossRef]
14. Jamil, M.I.; Wang, Q.; Ali, A.; Hussain, M.; Aziz, T.; Zhan, X.; Zhang, Q. Slippery Photothermal Trap for Outstanding Deicing Surfaces. *J Bionic Eng* **2021**, *18*, 548–558. [CrossRef]

15. Guo, P.; Zheng, Y.; Wen, M.; Song, C.; Lin, Y.; Jiang, L. Icephobic/Anti-Icing Properties of Micro/Nanostructured Surfaces. *Adv. Mater.* **2012**, *24*, 2642–2648. [CrossRef] [PubMed]
16. Wang, L.; Gong, Q.; Zhan, S.; Jiang, L.; Zheng, Y. Robust Anti-Icing Performance of a Flexible Superhydrophobic Surface. *Adv. Mater.* **2016**, *28*, 7729–7735. [CrossRef]
17. Shen, Y.; Wang, G.; Tao, J.; Zhu, C.; Liu, S.; Jin, M.; Xie, Y.; Chen, Z. Anti-Icing Performance of Superhydrophobic Texture Surfaces Depending on Reference Environments. *Adv. Mater. Interfaces* **2017**, *4*, 1700836. [CrossRef]
18. Jung, S.; Dorrestijn, M.; Raps, D.; Das, A.; Megaridis, C.M.; Poulikakos, D. Are Superhydrophobic Surfaces Best for Icephobicity? *Langmuir* **2011**, *27*, 3059–3066. [CrossRef]
19. Chen, C.; Tian, Z.; Luo, X.; Jiang, G.; Hu, X.; Wang, L.; Peng, R.; Zhang, H.; Zhong, M. Cauliflower-like Micro-Nano Structured Superhydrophobic Surfaces for Durable Anti-Icing and Photothermal de-Icing. *Chem. Eng. J.* **2022**, *450*, 137936. [CrossRef]
20. Xie, Z.; Wang, H.; Geng, Y.; Li, M.; Deng, Q.; Tian, Y.; Chen, R.; Zhu, X.; Liao, Q. Carbon-Based Photothermal Superhydrophobic Materials with Hierarchical Structure Enhances the Anti-Icing and Photothermal Deicing Properties. *ACS Appl. Mater. Interfaces* **2021**, *13*, 48308–48321. [CrossRef]
21. Zhao, Y.; Yan, C.; Hou, T.; Dou, H.; Shen, H. Multifunctional Ti3C2Tx MXene-Based Composite Coatings with Superhydrophobic Anti-Icing and Photothermal Deicing Properties. *ACS Appl. Mater. Interfaces* **2022**, *14*, 26077–26087. [CrossRef]
22. Hou, M.; Jiang, Z.; Sun, W.; Chen, Z.; Chu, F.; Lai, N.-C. Efficient Photothermal Anti-/Deicing Enabled by 3D Cu2-xS Encapsulated Phase Change Materials Mixed Superhydrophobic Coatings. *Adv. Mater.* **2024**, *36*, 2310312. [CrossRef]
23. Sun, W.; Wei, Y.; Feng, Y.; Chu, F. Anti-Icing and Deicing Characteristics of Photothermal Superhydrophobic Surfaces Based on Metal Nanoparticles and Carbon Nanotube Materials. *Energy* **2024**, *286*, 129656. [CrossRef]
24. Jiang, G.; Chen, L.; Zhang, S.; Huang, H. Superhydrophobic SiC/CNTs Coatings with Photothermal Deicing and Passive Anti-Icing Properties. *ACS Appl. Mater. Interfaces* **2018**, *10*, 36505–36511. [CrossRef]
25. Xie, Z.; Wang, H.; Li, M.; Tian, Y.; Deng, Q.; Chen, R.; Zhu, X.; Liao, Q. Photothermal Trap with Multi-Scale Micro-Nano Hierarchical Structure Enhances Light Absorption and Promote Photothermal Anti-Icing/Deicing. *Chem. Eng. J.* **2022**, *435*, 135025. [CrossRef]
26. Xie, H.; Xu, W.-H.; Du, Y.; Gong, J.; Niu, R.; Wu, T.; Qu, J.-P. Cost-Effective Fabrication of Micro-Nanostructured Superhydrophobic Polyethylene/Graphene Foam with Self-Floating, Optical Trapping, Acid-/Alkali Resistance for Efficient Photothermal Deicing and Interfacial Evaporation. *Small* **2022**, *18*, 2200175. [CrossRef]
27. Xie, H.; Wei, J.; Duan, S.; Zhu, Q.; Yang, Y.; Chen, K.; Zhang, J.; Li, L.; Zhang, J. Non-Fluorinated and Durable Photothermal Superhydrophobic Coatings Based on Attapulgite Nanorods for Efficient Anti-Icing and Deicing. *Chem. Eng. J.* **2022**, *428*, 132585. [CrossRef]
28. Miao, S.; Liu, X.; Chen, Y. Freezing as a Path to Build Micro-Nanostructured Icephobic Coatings. *Adv. Funct. Mater.* **2023**, *33*, 2212245. [CrossRef]
29. Jamil, M.I.; Zhan, X.; Chen, F.; Cheng, D.; Zhang, Q. Durable and Scalable Candle Soot Icephobic Coating with Nucleation and Fracture Mechanism. *ACS Appl. Mater. Interfaces* **2019**, *11*, 31532–31542. [CrossRef]
30. Xu, Y.; Zhang, G.; Li, L.; Xu, C.; Lv, X.; Zhang, H.; Yao, W. Icephobic Behaviors of Superhydrophobic Amorphous Carbon Nano-Films Synthesized from a Flame Process. *J. Colloid Interface Sci.* **2019**, *552*, 613–621. [CrossRef]
31. Wu, S.; Du, Y.; Alsaid, Y.; Wu, D.; Hua, M.; Yan, Y.; Yao, B.; Ma, Y.; Zhu, X.; He, X. Superhydrophobic Photothermal Icephobic Surfaces Based on Candle Soot. *Proc. Natl. Acad. Sci. USA* **2020**, *117*, 11240–11246. [CrossRef]
32. MacNeil, J.; Volaric, L. Incomplete Combustion with Candle Flames: A Guided-Inquiry Experiment in the First-Year Chemistry Lab. *J. Chem. Educ.* **2003**, *80*, 302. [CrossRef]
33. Liang, C.-J.; Liao, J.-D.; Li, A.-J.; Chen, C.; Lin, H.-Y.; Wang, X.-J.; Xu, Y.-H. Relationship between Wettabilities and Chemical Compositions of Candle Soots. *Fuel* **2014**, *128*, 422–427. [CrossRef]
34. Qahtan, T.F.; Gondal, M.A.; Alade, I.O.; Dastageer, M.A. Fabrication of Water Jet Resistant and Thermally Stable Superhydrophobic Surfaces by Spray Coating of Candle Soot Dispersion. *Sci. Rep.* **2017**, *7*, 7531. [CrossRef]
35. Garbassi, F.; Balducci, L.; Chiurlo, P.; Deiana, L. A Study of Surface Modification of Silica Using XPS, DRIFT and NMR. *Appl. Surf. Sci.* **1995**, *84*, 145–151. [CrossRef]
36. Yang, C.; Tartaglino, U.; Persson, B.N.J. Influence of Surface Roughness on Superhydrophobicity. *Phys. Rev. Lett.* **2006**, *97*, 116103. [CrossRef] [PubMed]
37. Wu, Y.; Wang, J.; Zhang, D.; Li, L.; Zhu, Y. Preparation and Characterization of Superhydrophobic Surface Based on Polydimethylsiloxane (PDMS). *J. Adhes. Sci. Technol.* **2019**, *33*, 1870–1881. [CrossRef]
38. Zheng, Q.; Lü, C. Size Effects of Surface Roughness to Superhydrophobicity. *Procedia IUtam* **2014**, *10*, 462–475. [CrossRef]
39. Das, A.; Shome, A.; Manna, U. Porous and Reactive Polymeric Interfaces: An Emerging Avenue for Achieving Durable and Functional Bio-Inspired Wettability. *J. Mater. Chem. A* **2021**, *9*, 824–856. [CrossRef]
40. Dash, S.; de Ruiter, J.; Varanasi, K.K. Photothermal Trap Utilizing Solar Illumination for Ice Mitigation. *Sci. Adv.* **2018**, *4*, eaat0127. [CrossRef]
41. Marín, A.G.; Enríquez, O.R.; Brunet, P.; Colinet, P.; Snoeijer, J.H. Universality of Tip Singularity Formation in Freezing Water Drops. *Phys. Rev. Lett.* **2014**, *113*, 054301. [CrossRef] [PubMed]
42. Graeber, G.; Schutzius, T.M.; Eghlidi, H.; Poulikakos, D. Spontaneous Self-Dislodging of Freezing Water Droplets and the Role of Wettability. *Proc. Natl. Acad. Sci. USA* **2017**, *114*, 11040–11045. [CrossRef] [PubMed]

43. Snoeijer, J.H.; Brunet, P. Pointy Ice-Drops: How Water Freezes into a Singular Shape. *Am. J. Phys.* **2012**, *80*, 764–771. [CrossRef]
44. Jung, S.; Tiwari, M.K.; Poulikakos, D. Frost Halos from Supercooled Water Droplets. *Proc. Natl. Acad. Sci. USA* **2012**, *109*, 16073–16078. [CrossRef]
45. Liu, Y.; Wu, Y.; Liu, Y.; Xu, R.; Liu, S.; Zhou, F. Robust Photothermal Coating Strategy for Efficient Ice Removal. *ACS Appl. Mater. Interfaces* **2020**, *12*, 46981–46990. [CrossRef]
46. Xue, C.-H.; Li, H.-G.; Guo, X.-J.; Ding, Y.-R.; Liu, B.-Y.; An, Q.-F.; Zhou, Y. Superhydrophobic Anti-Icing Coatings with Self-Deicing Property Using Melanin Nanoparticles from Cuttlefish Juice. *Chem. Eng. J.* **2021**, *424*, 130553. [CrossRef]
47. Boinovich, L.B.; Emelyanenko, A.M. Recent Progress in Understanding the Anti-Icing Behavior of Materials. *Adv. Colloid Interface Sci.* **2024**, *323*, 103057. [CrossRef]
48. Hu, H.; Larson, R.G. Marangoni Effect Reverses Coffee-Ring Depositions. *J. Phys. Chem. B* **2006**, *110*, 7090–7094. [CrossRef] [PubMed]
49. Wang, W.; Han, B.; Zhang, Y.; Li, Q.; Zhang, Y.-L.; Han, D.-D.; Sun, H.-B. Laser-Induced Graphene Tapes as Origami and Stick-On Labels for Photothermal Manipulation via Marangoni Effect. *Adv. Funct. Mater.* **2021**, *31*, 2006179. [CrossRef]
50. Wang, X.; Lu, Y.; Zhang, Q.; Wang, K.; Carmalt, C.J.; Parkin, I.P.; Zhang, Z.; Zhang, X. Durable Fire Retardant, Superhydrophobic, Abrasive Resistant and Air/UV Stable Coatings. *J. Colloid Interface Sci.* **2021**, *582*, 301–311. [CrossRef]